PAPER

Micro-trench measurements of the net deposition of carbon impurity ions in the DIII-D divertor and the resulting suppression of surface erosion

To cite this article: S Abe et al 2021 Phys. Scr. 96 124039

View the article online for updates and enhancements.

You may also like

- ERO modeling and analysis of tungsten erosion and migration from a toroidally symmetric source in the DIII-D divertor
 J. Guterl, T. Abrams, C.A. Johnson et al.
- <u>Single- and Multi-Directional Slanted</u>
 <u>Plasma Etching of Silicon under Practical</u>
 <u>Plasma Processing Conditions</u>
 <u>Sung-Woon Cho, Jun-Hyun Kim, Doo Won</u>
 Kang et al.
- Advances in understanding of high-Z material erosion and re-deposition in low-Z wall environment in DIII-D R. Ding, D.L. Rudakov, P.C. Stangeby et

Physica Scripta



RECEIVED 19 June 2021

17 June 20

REVISED 13 September 2021

ACCEPTED FOR PUBLICATION 28 September 2021

PUBLISHED
11 October 2021

PAPER

Micro-trench measurements of the net deposition of carbon impurity ions in the DIII-D divertor and the resulting suppression of surface erosion

S Abe^{1,*}, C H Skinner², I Bykov³, J Guterl⁴, A Lasa⁵, Y W Yeh⁶, J Coburn⁷, D L Rudakov³, C J Lasnier⁸, H Q Wang⁴, A G McLean⁸, T Abrams⁴ and B E Koel¹

- ¹ Department of Chemical and Biological Engineering, Princeton University, Princeton, NJ 08540, United States of America
- ² Princeton Plasma Physics Laboratory, Princeton, NJ 08543, United States of America
- ³ Center for Energy Research, University of California San Diego, CA 92093, United States of America
- General Atomics, San Diego, CA 92186, United States of America
- ⁵ University of Tennessee, Knoxville, TN 37996, United States of America
- ⁶ Department of Physics and Astronomy, Rutgers, The State University of New Jersey, Piscataway, NJ 08854, United States of America
- Sandia National Laboratory, Livermore, CA 94550, United States of America
- ⁸ Lawrence Livermore National Laboratory, Livermore, CA, 94550, United States of America
- * Author to whom any correspondence should be addressed.

E-mail: shotaa@princeton.edu

Keywords: Plasma-material interaction, Carbon Impurity, Ion incident angle, Erosion, Deposition, Divertor, Surface analysis

Abstract

We report carbon impurity ion incident angles and deposition rates, along with silicon erosion rates, from measurements of micro-engineered trenches on a silicon surface exposed to L-mode deuterium plasmas at the DIII-D divertor. Post exposure *ex-situ* analysis determined elemental maps and concentrations, carbon deposition thicknesses, and erosion of silicon surfaces. Carbon deposition profiles on the trench floor showed carbon ion shadowing that was consistent with ERO calculations of average carbon ion angle distributions (IADs) for both polar and azimuthal angles. Measured silicon net erosion rates negatively correlated with the deposited carbon concentration at different locations. Differential erosion of surfaces on two different ion-downstream trench slope structures suggested that carbon deposition rate is affected by the carbon ion incident angle and significantly suppressed the surface erosion. The results suggest the C impurity ion incident angles, determined by the IADs and surface morphology, strongly affect erosion rates as well as the main ion (D, T, He) incident angles.

1. Introduction

Low-Z impurities, such as C and Be, can play an important role in the erosion of high-Z materials in tokamak plasma devices. In H-mode operations with edge localized modes (ELMs), erosion in the divertor is dominated by physical sputtering enhanced by impurities, e.g., C for DIII-D [1, 2] and ASDEX Upgrade [3], and Be for JET [4, 5]. On the contrary, C deposition on plasma-facing component (PFC) surfaces reduces the effective sputtering rate of Mo and W due to deposited C diluting the material surface in L-mode DIII-D discharges [6]. Similar calculation results of W erosion suppression were reported for L-mode EAST discharges when the C impurity concentration was higher than 1% [7, 8]. Hence, the characteristics of those low-Z impurities such as deposition rate, concentration in the plasma, and incident angle and energy comprise crucial information needed to understand the net erosion of PFCs. Modeling using the ERO 3D-Monte Carlo code and simple equation-of-motion models showed that the sheath width is a critical parameter controlling the incident ion trajectory of C [9] as well as D and He ions [10, 11]. Calculations have also shown that the incident ion angles of C [9], Be, and N [12] impurities are more affected by the sheath than that of the main D species.

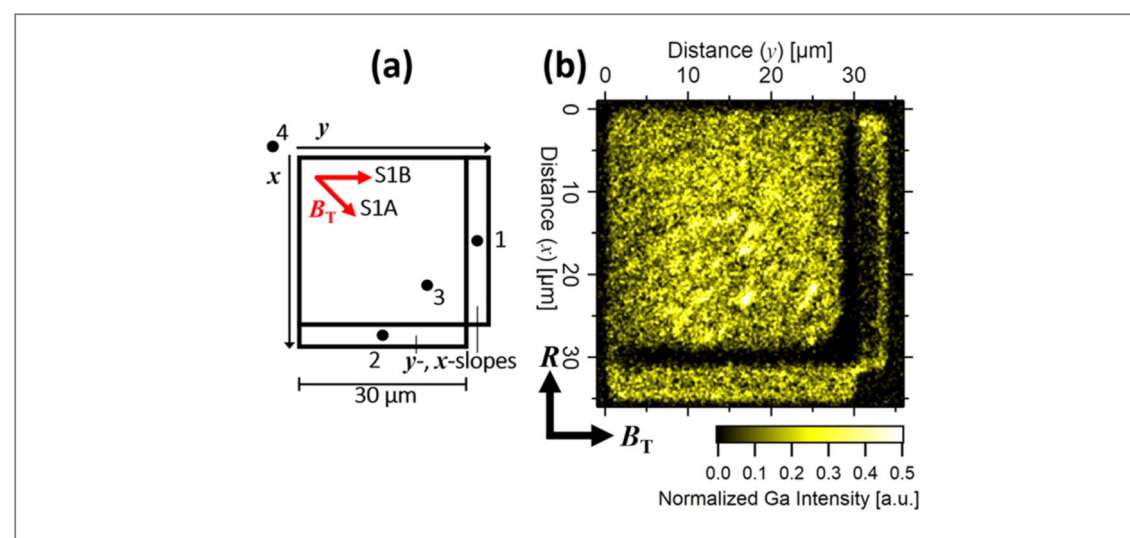


Figure 1. (a) Schematic of a trench indicating B_T directions, sloped walls, trench coordinates (x-y), and point locations (\cdot 1-4) used for analysis. (b) Ga EDS map of trench **T42** on **S1B**, with major radius R and toroidal field B_T directions indicated. The 1–2 μ m wide dark region on the floor seen at the bottom and right sides, just next to trench walls, arises because x-rays from that region are blocked by the trench walls.

We have previously reported experimental measurements of the polar and azimuthal D ion angle distributions (IADs) at the divertor surface in DIII-D using $30 \times 30 \times 2$ –4 μm deep micro-trenches [11, 13]. These sample surfaces were exposed to L-mode D discharges using the Divertor Materials Evaluation System (DiMES) facility [14] at DIII-D. Deposition patterns of C impurities on the trench floors resulting from D incident ion shadowing effects from the trench walls were measured by energy-dispersive X-ray spectroscopy (EDS) and compared with a net erosion calculated by the Monte Carlo micro-patterning and roughness (MPR) code [15, 16]. The C EDS intensity profiles showed that trench floor erosion was maximized at the azimuthal direction of $\varphi = -40^{\circ}$ (referenced to $\varphi = 0^{\circ}$ for the toroidal magnetic field) and polar angle of $\theta = 80^{\circ}$ (referenced to $\theta = 0^{\circ}$ for the surface normal), in which the incident angle of the magnetic field onto the surface was $\alpha = 88.5^{\circ}$ (referenced to the surface normal). A schematic of the spherical coordinate system employed for this article is shown in figure 1(b) of reference [10]. The MPR code reproduced the erosion pattern by using D IADs, which have average values of $\varphi = -40^{\circ}$ and $\theta = 80^{\circ}$, calculated by an analytical equation-of-motion model [10, 17] for the case k = 3 and $L_{MPS} = k \times \rho_i(\rho_i$; the ion gyro radius), when the sheath potential was analytically approximated by $\phi = \phi_w \exp(-2z/L_{MPS})$ (ϕ_w ; the potential drop at the wall measured from the entrance of the sheath, z; the distance from the surface).

In this paper we report on the accumulation of C impurities in D ion shadowed areas of the micro-trenches and Si erosion at various locations on the Si disc DiMES samples. The micro-trench technique revealed the effect of C redeposition on Si erosion from the sample, which benchmarks the previous DiMES experiments and ERO calculations for Mo and W [6]. Carbon deposition profile and thickness in the D ion shadowing area on the trench floor, C impurity concentrations at different locations, and erosion of the trenches were analyzed after exposure to L-mode D discharges. Sputtering and deposition of materials were calculated by the MPR code, which uses the experimentally verified polar and azimuthal D IADs and calculated average C IADs.

2. Experiment

A schematic drawing of the Si samples with trench locations was shown in a previous report (figure 1 of [13]). Micro-trenches $30 \, \mu m \times 30 \, \mu m \times 2-4 \, \mu m$ deep were fabricated on the 'downstream' half of the Si sample surface relative to the toroidal magnetic field, B_T , direction by a focused ion beam (FIB) etching system that used Ga ions at 30 keV as described in a previous report [13]. FIB etching formed a Ga-implanted Si layer 28-nm thick, which was calculated by SRIM [18] for the penetration range, i.e., peak concentration depths, of 30-keV Ga ions in Si, at the trench floor and wall surfaces. The layer will be used as a reference property of the original trench surface so that morphology changes before and after plasma exposures can be analyzed. We use data from the two samples reported in [11, 13] that were located at the center of the DiMES head and indicated as 'S1' in [13]. Configurations of the samples and trenches used in this analysis are summarized in table 1. We refer to the samples reported in [13] and [11] as 'S1A' and 'S1B', respectively. The trenches reported herein are denoted as T31 and T32 (3- μ m deep) on S1A (figure 1 in [13]), and T41 and T42 (4- μ m deep) on S1B. T42 is the trench T4 reported in [11] located at the same position as T32 (0.5 mm from the DiMES head boundary), and T41 and T31

Phys. Scr. **96** (2021) 124039

Table 1. Summary of C net deposition and Si net erosion for four trench configurations. Si erosion depth was measured by AFM, and C concentrations at locations outside the trench were measured by EDS.

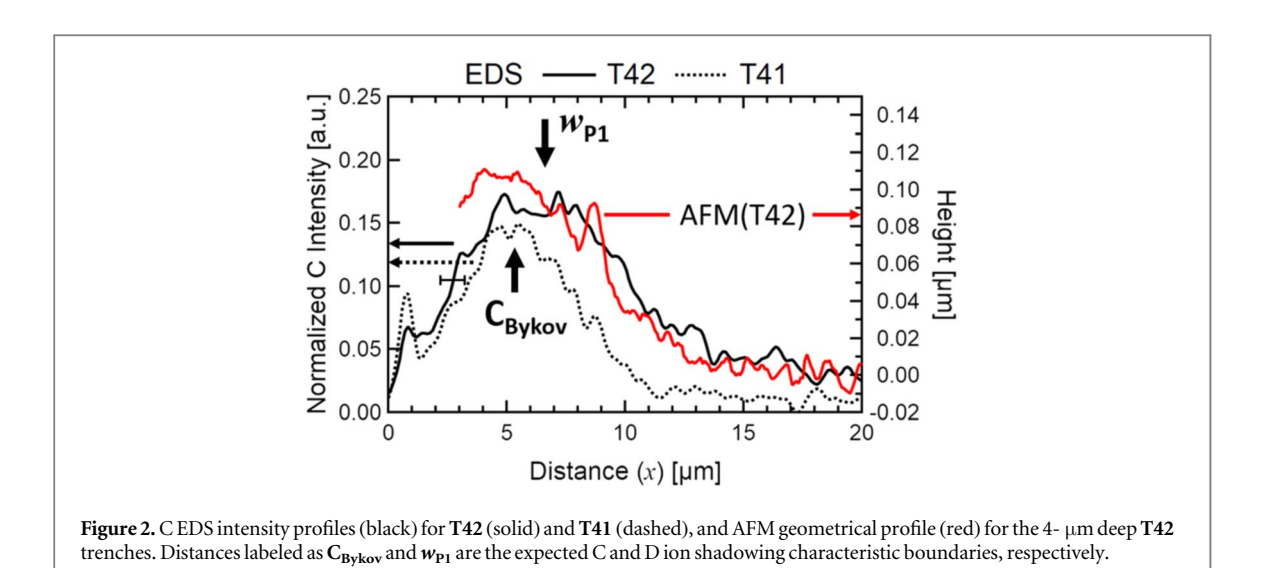
Trench	T42	T32	T41	T31		
Sample Disc	S1B	S1A	S1B	S1A		
y Direction (φ)	0°	45°	0°	45°		
Depth [μm]	4	3	4	3		
Distance from DiMES Head [mm]	0.5	0.5	2	2		
Exposure Time [s]	10	30	10	30		
C Net Deposition (± 30) [nm]	110	300	100	280		
C Net Deposition Rate [nm s ⁻¹]	11 ± 3	10 ± 1	10 ± 3	9.3 ± 1		
	10.5	(avg.)	9.7 (avg.)			
Si Net Erosion (± 30) [nm] at position 4	38	100	53	170		
Si Net Erosion Rate [nm s ⁻¹]	3.8 ± 3	3.3 ± 1	5.3 ± 3	5.7 ± 1		
	3.5 (avg.)	5.5 (avg.)			
C Concentration [%] at position 4	5.4 ± 0.1	5.4 ± 0.2	4.1 ± 0.2	4.9 ± 0.3		
	5.4 (avg.)	4.5 (avg.)			
Si Net Erosion (± 30) [nm] at position 3	_	_	_	110		
Si Net Erosion Rate [nm s ⁻¹]	_	_	_	3.7 ± 1		
C Concentration [%] at position 3	9 ± 1.6	8.7 ± 0.2	5.4 ± 0.4	4.9 ± 0.2		
	8.8 (avg.)	5.2 (avg.)			

are located in the inner trench array (2 mm from the DiMES head boundary). The main difference between samples **S1A** and **S1B** is the trench orientation: the **S1B** trenches were rotated clockwise by 45° in the x-y plane compared to the **S1A** trenches. Figure 1(a) shows a schematic of the B_T directions, sloped walls on the ion downstream sides, trench coordinates (x-y), and locations used for analysis. A geometrical profile measured by atomic force microscopy (AFM) before exposure, and a scanning electron microscopy (SEM) image after exposure, of a 3- μ m deep trench on **S1A** are shown in figure 2 and 3 of [13], respectively. The slope structures on the ion downstream sides are seen in both figures, and AFM measurements indicated the slope tilt was ~20° from the horizontal plane. We identify those slope structures as the x-slope (marked as \cdot 1) and y-slope (marked as \cdot 2) in figure 1(a).

The samples were exposed to steady-state L-mode D plasmas characterized by electron temperature $T_{\rm e} \sim 30$ eV, electron density $n_{\rm e} \sim 0.7 \times 10^{13}$ cm⁻³, ion flux $I \sim 10^{18}$ cm⁻² s⁻¹ perpendicular to the divertor surface, $B_T = 2.0$ T, and a B incident angle $\alpha = 88.5^{\circ}$. Total exposure times were 30 s (L-mode shots: #179785-87, 179789-93) for S1A and 10 s (L-mode shots: #182505, 182506, and 182508) for S1B. The C impurity concentration in the plasmas was estimated to be 1.2% for similar discharge parameters ('S-D Case' in [10]) by an ERO calculation [19] and we assume a similar C ion concentration in the experiments considered herein. UEDGE modeling of C^{x+} ion fractions in a H-mode plasma in DIII-D showed C^{2+} and C^{3+} were the dominant species, with fractions of C^+ and C^{4+} one order of magnitude smaller [19]. We examine the C^+ and C^{3+} species to evaluate the effect of the C ion charge states on redeposition in section 4. We assign experimental errors for the azimuthal and polar angles as $\pm 3^\circ$ and $\pm 1^\circ$, respectively, herein due to the experimental uncertainty in mounting the sample in the DiMES head. Post-exposure ex-situ analysis was performed using SEM, EDS, and AFM as described previously [13]. The electron energy for EDS was chosen to be 5.0 keV, at which the penetration depth in Si is 200 nm [20]. EDS concentration analysis was performed three times by slightly shifting the target position within a 1 μm distance at each location. Averaged values are used for each location, and standard deviations are indicated by the error bars. 2D elemental deposition maps and 1D line profiles using the EDS signals were generated by the same procedure as described previously [13].

3. Computational model

A Monte Carlo MPR code [15, 16, 21] was used to model physical sputtering and C impurity deposition due to D and C ion bombardment on the trench Si surfaces or deposited C layers. 3D geometries of the trenches were mathematically reproduced (as shown in figure 2 of [13]) and used as input to the MPR code. We used the azimuthal and polar D IADs for k=3, which were verified experimentally with an uncertainty of ± 0.5 [11], to set up the flux of D ions. We employed a single ion direction, $\theta=60^{\circ}$ and $\varphi=-55^{\circ}$, taken from average C (C^{x+} : x=1-3) IADs calculated by ERO assuming k=2.4 [9], to set up the C ion flux. Both energy and angular dependencies of sputtering and reflection rate coefficients were the same as those in [13] for D ion projectiles. We used sputtering and reflection rate coefficients from [22, 23] for C ion bombardment on C. The incident ion energies, E_{impact} , employed for calculations were 140 eV for D⁺ and C⁺, and 300 eV for C³⁺, by assuming



 $E_{\rm impact} \sim 3Z_{\rm i}kT_{\rm e} + 2kT_{\rm i}$ and $T_{\rm e} \sim T_{\rm i}$ [13, 24]. A value of 140 eV for singly ionized species was employed rather than 150 eV because of the availability of rate coefficients.

4. Results and discussion

4.1. C accumulation on the trench floors

EDS intensity maps of samples **S1A** and **S1B** reveal deposition patterns of elements, including C, on the trench floors and were reported in [13] and [11], respectively. Figure 2 shows a C intensity line profile from **S1B** trenches measured by EDS along the *x*-direction (defined in figure 1) at $y = 20 \,\mu\text{m}$ averaged over a $10 \,\mu\text{m}$ wide band. The C intensity increases as a function of distance from the upstream wall and is maximized at $x \sim 5 \,\mu\text{m}$. This distance is consistent with the shadowing boundary of the averaged C IAD calculated by Guterl [9], $x = 5.5 \,\mu\text{m}$ (C_{Bykov} in figure 2), and the C accumulation direction on C micro-spheres recently measured by Bykov [25]. The C intensity is fairly uniform in the range $x \sim 5$ –7 μm , especially for **T42**. The decay after $x \sim 6$ –7 μm (w_{P1} in figure 2) is due to sputtering by the D ions having shallower incident angle than C ions [13]. The same trend for the C peak location for the **T32** and **T31** trenches was seen in figure 6(a) of [13], where the C EDS profiles had maxima at $x \sim 5 \,\mu\text{m}$, consistent with the average C ion shadowing boundary for those trenches that was expected at $x = 5 \,\mu\text{m}$. The continuous C intensity profiles near the upstream wall (x = 0–5 μ m) for those four trenches indicate broad C IADs [9]. We note that there can also be impurity C ions promptly redeposited [13] from the DiMES graphite head, and that C neutrals may be more uniformly deposited than C ions.

The Ga EDS intensity map for **T42** in figure 1(b) shows the presence of Ga everywhere in the trench except for the x-slope region. This means that the implanted Ga layer (the original trench floor) was not completely eroded away by the plasma exposure except for in the x-slope region. This is in contrast to the Ga EDS intensity map for **T31** shown in figure 5(b) of [13]. The Ga EDS intensity in [13] is visible in the area near $x = 10 \,\mu\text{m}$ from the upstream wall and there is a darker region around the upstream wall and downstream region (upper half of the EDS map). This indicates that deposited C covered the Ga-containing top layer in the D-ion shadowed region, while D ions sputtered the Ga-containing layer away in the downstream area. The difference between the Ga profiles for the T42 and T32 trenches arose because the Ga-rich layer on the entire floor of T42 survived the short 10-s plasma exposure time, but the Ga-rich layer for the T32 case was partially eroded by the 30-s plasma exposure. The area with well-pronounced Ga intensity can be used as a reference for the original Ga-rich trench surface. AFM measurements shown in figure 2 found a geometrical profile change of the T42 trench floor after plasma exposure. The profile shown was obtained by subtracting an AFM profile of the **T42** trench before exposure from an AFM profile of the same trench after exposure to reveal the morphology changes. The AFM height of the area where Ga EDS intensity was high ($x > 15 \mu m$ for T42) and C deposition was low (confirmed by C EDS intensity), was set to a value of 'zero' to indicate the height of the original trench surface. The main uncertainty in the height obtained by this method of calibration is from the thickness of the original Ga-rich layer, \sim 30 nm. The AFM profile of the **T42** trench was consistent with the C EDS profile, especially in the range x > 7 µm. This indicates that the deposition on the trench floor consists mainly of C. The maximum height due to C deposition measured within each trench is summarized in table 1. A height of ~ 100 nm was measured for the S1B samples (T41 and T42), and \sim 300 nm was measured for the S1A samples (T31 and T32). The results are

consistent with the ion fluence on each sample, since the **S1B** exposure time was about three times longer than for **S1A**. The thickness of \sim 300 nm is also relevant to a deposited C layer of \sim 200 nm thickness that was measured on a carbon-sphere [25] using the same plasmas and exposure time as for **S1A**. Thicker C deposition layers were measured in our case because these C layers were measured in the D ion-shadowed region, while the C accumulated on the micro-spheres was directly exposed to D ions, causing some re-erosion. The C deposition rate measured by the trench technique was \sim 10 nm s⁻¹ perpendicular to the sample surface.

4.2. Erosion suppression by C impurity deposition

Measurements of the trench morphologies with AFM can determine the Si net erosion rate. The height of the surface outside the trenches was measured relative to the Ga-rich layer on the trench floor before and after plasma exposure. These height differences were used to determine the net Si erosion rate outside the trenches. The results are summarized in table 1. The measured Si net erosion rates were 3.5 nm s $^{-1}$ for trenches **T32** and T42 and 5.5 nm s⁻¹ for trenches T31 and T42. Interestingly, for both S1A and S1B, different erosion rates were measured at different locations on the same sample. Table 1 also shows the C concentration (at%) outside the trenches as measured by EDS. The C concentrations for T32 and T42 located nearer to the edge of the sample discs and closer to the DiMES head were 5.5%, which is higher than the 4.5% for T31 and T41 located at the middle of the sample discs. Such a C concentration gradient as a function of distance from the DiMES head boundary is consistent with the analysis made previously [13]. Modelling by Ding et al [6] showed previously that the net erosion of Mo was suppressed by 20%–50% when the surface C concentration increased by 20% in a typical C impurity concentration range of 1%–2% in the background plasma. Such a correlation between C concentration and Si erosion rate can also be seen in the experiment reported herein. SiC formation due to C ion bombardment on the Si surface may also be a factor, since SDTrimSP [26] calculations give that SiC has an order or magnitude smaller sputtering yield than amorphous Si:C for 150 eV D ions [27]. The C ion penetration ranges for 150 eV and 300 eV at normal incidence calculated by SRIM [18] are 1.5 and 2.2 nm, respectively. Si net erosion on the trench floor, in areas beyond the Dion shadowing limit, was also measured and is shown in table 1. The measured Si net erosion for trenches T42, T32, and T41 was zero within the error bars. We see the erosion rate for T31 is lower than the rate outside the trench. Those results suggest suppression of Si erosion from the trench floor occurred because the C concentrations in these areas were 15%–60% higher than outside the trench.

EDS analysis for the **T42** and **T41** trenches indicated that the Ga layer survived on one of the downstream slopes, which was not shadowed from either C or D ions, as shown in figure 1(b). No Ga layers were seen on the sloping sidewalls of **T32** and **T31**, possibly due to the long exposure time. Figure 1(b) shows the Ga-implanted layer on the x-slope of **T42** was eroded away, but it survived on the y-slope of **T42**. Table 2 shows results from MPR calculations of the sputtering rate of Si due to D ion bombardment at the different locations indicated in figure 1, normalized to the sputtering rate outside the trench at location **4**. The sputtering rate on the trench slopes were calculated to be about eight times higher than outside the trench due to enhancement of the incident ion flux [ions/s·m²] and the sputtering yield [atoms/ion] by steeper ion incident angles. Therefore, the erosion of those slopes would be expected to be much larger than the Ga-implanted layer thickness.

This suggests some mechanism prevented Ga erosion at the y-slope (at location 2) of trenches T42 and T41. Table 2 shows that the Ga concentration has a positive correlation with the redeposited C concentration after exposure. C concentrations on the y-slopes are 20%–50% higher than on the x-slopes and outside surfaces for each trench. MPR calculations for C ion bombardment on C layers were performed to understand this C redeposition behavior. These calculations show that the ion flux is enhanced at both the x- and y-slopes due to the steeper incident angles made by the slope geometry. If we multiply the ion flux by the effective deposition yield, given by $(1 - R_N) - Y_{phys}$, where R_N is the reflection yield [atoms/ion] and Y_{phys} is the sputtering yield [atoms/ion], we obtain the effective deposition rate as a function of the incident angle, which is shown in table 2. These calculations found that C deposition was larger on the y-slope by 40% for C^+ and 210% for C^{3+} incident ions, relative to the x-slope. The ratio of the C concentrations on the y-slope and x-slope were measured to be 40%–50% in both **T42** and **T41**. The negative deposition rate (i.e., net erosion rate) of C^{3+} indicates that sputtering by C incident ions dominates C deposition on the flat surfaces (Locations 3 and 4). Hence, C accumulation seen in the D ion-shadowed area may be mainly due to incident C^+ (or C^{2+}) ions. However, because we do not have more detailed information about the C ion charge states and their background plasma concentrations, quantitative analysis will be left to future studies using 3D Monte Carlo modeling codes such as ERO or GITR [28, 29]. Nevertheless, these results qualitatively explain the significant suppression of net erosion of trench y-slopes. This underscores the importance of understanding the balance between net erosion and deposition of low-Z material, which is affected not only by the impurity fractions and their charge states (energy), and also by the incident ion directions and surface morphology of the PFCs.

Table 2. Summary of C and Ga concentrations at different locations measured by EDS, and sputtering yields and deposition rates calculated by MPR. More Ga (less erosion) was detected, and higher C deposition was calculated, on the *y*-slope relative to the *x*-slope. The retention yield is defined as - $R_{\rm N}$.

EDS (exp.)			MPR (calc.)										
T	42	T42 T42,T41 [%] Concentration [%] D+(140 eV)→Si		12, T41	T42, T41								
Concenti	ration [%]			D ⁺ (140 eV)→Si				C ⁺ (140 eV)→C			C ³⁺ (300 eV)→C		
С	Ga	С	Ga	Avg. Impact Angle	Norm. Sput- tering Rate	Impact Angle	Norm. Flux	Retention Yield [/ion]	Sputtering Yield [/ion]	Deposition Rate [a.u.]	Retention Yield [/ion]	Sputtering Yield [/ion]	Deposition Rate [a.u.]
6.4 ± 0.5	0.7 ± 0.4	3.5 ± 0.1	0.0 ± 0.0	63°	7.5	48°	1.5	0.9	0.28	0.93	0.76	0.53	0.35
9 ± 1	$\textbf{4.7}\pm0.4$	5.2 ± 0.2	2.9 ± 0.1	66°	8.6	40°	1.7	0.95	0.19	1.29	0.81	0.37	0.75
9 ± 1.6 5.4 ± 0.1	4.7 ± 0.8	5.4 ± 0.4 4.1 ± 0.2	3 ± 1	80° 80°	1	60°	1	0.76	0.41	0.35	0.61	0.8	-0.19
	Concentro C 6.4 ± 0.5 9 ± 1	T42 Concentration [%] C Ga 6.4 ± 0.5 0.7 ± 0.4 9 ± 1 4.7 ± 0.4 9 ± 1.6 4.7 ± 0.8	$ \begin{array}{c ccccccccccccccccccccccccccccccccccc$	T42 Concentration [%] Concentration [%] C Ga C Ga 6.4 ± 0.5 0.7 ± 0.4 3.5 ± 0.1 0.0 ± 0.0 9 ± 1 4.7 ± 0.4 5.2 ± 0.2 2.9 ± 0.1 9 ± 1.6 4.7 ± 0.8 5.4 ± 0.4 3 ± 1	$ \begin{array}{c ccccccccccccccccccccccccccccccccccc$	T42 T42, T41 Concentration [%] Concentration [%] D ⁺ (140 eV)→Si Avg. Impact Norm. Sputtering Rate C Ga C Ga Angle tering Rate 6.4 ± 0.5 0.7 ± 0.4 3.5 ± 0.1 0.0 ± 0.0 63° 7.5 9 ± 1 4.7 ± 0.4 5.2 ± 0.2 2.9 ± 0.1 66° 8.6 9 ± 1.6 4.7 ± 0.8 5.4 ± 0.4 3 ± 1 80° 1	$\begin{array}{c ccccccccccccccccccccccccccccccccccc$	$ \begin{array}{c ccccccccccccccccccccccccccccccccccc$	T42 T42 T41 Concentration [%] Concentration [%] D ⁺ (140 eV)→Si Avg. Impact Norm. Sput- Impact Angle Flux Yield [/ion] 6.4 ± 0.5 0.7 ± 0.4 3.5 ± 0.1 0.0 ± 0.0 63° 7.5 48° 1.5 0.9 9 ± 1 4.7 ± 0.4 5.2 ± 0.2 2.9 ± 0.1 66° 8.6 40° 1.7 0.95 9 ± 1.6 4.7 ± 0.8 5.4 ± 0.4 3 ± 1 80° 1	T42 T42 T42, T41 Concentration [%] Concentration [%] D ⁺ (140 eV)→Si C ⁺ (140 eV)→C Avg. Impact Norm. Sput- Impact Norm. Sput- Impact Angle tering Rate Angle Flux Yield [/ion] Norm. Retention Sputtering Yield [/ion] 6.4 ± 0.5 0.7 ± 0.4 3.5 ± 0.1 0.0 ± 0.0 63° 7.5 48° 1.5 0.9 0.28 9 ± 1 4.7 ± 0.4 5.2 ± 0.2 2.9 ± 0.1 66° 8.6 40° 1.7 0.95 0.19 9 ± 1.6 4.7 ± 0.8 5.4 ± 0.4 3 ± 1 80° 1 60° 1 0.76 0.41	T42 T42, T41 T42, T41 Concentration [%] Concentration [%] D ⁺ (140 eV)→Si Limpact Norm. Sput- Angle Impact Flux Norm. Retention Yield [/ion] Sputtering Pate [/ion] Deposition Pate [a.u.] 6.4 ± 0.5 0.7 ± 0.4 3.5 ± 0.1 0.0 ± 0.0 63° 7.5 48° 1.5 0.9 0.28 0.93 9 ± 1 4.7 ± 0.4 5.2 ± 0.2 2.9 ± 0.1 66° 8.6 40° 1.7 0.95 0.19 1.29 9 ± 1.6 4.7 ± 0.8 5.4 ± 0.4 3 ± 1 80° 1 60° 1 0.76 0.41 0.35	$ \begin{array}{ c c c c c c c c c c c c c c c c c c c$	T42 T42, T41 T42, T41 Concentration [%] Concentration [%] D ⁺ (140 eV)→Si C ⁺ (140 eV)→C C ⁺ (140 eV)→C C ³⁺ (300 eV)→C C Ga C Ga Norm. Sput- Impact Angle tering Rate Norm. Retention Sputtering Plux Yield [/ion] Yield [/ion] Rate [a.u.] Pield [/ion] Yield [/ion] Yield [/ion] 6.4 ± 0.5 0.7 ± 0.4 3.5 ± 0.1 0.0 ± 0.0 63° 7.5 48° 1.5 0.9 0.28 0.93 0.76 0.53 0.53 9 ± 1 4.7 ± 0.4 5.2 ± 0.2 2.9 ± 0.1 66° 8.6 40° 1.7 0.95 0.19 1.29 0.81 0.37 9 ± 1.6 4.7 ± 0.8 5.4 ± 0.4 3 ± 1 80° 1 60° 1 0.76 0.41 0.35 0.61 0.8

5. Summary

In order to investigate C impurity ion incident angles in the DIII-D divertor and obtain new information about PFC erosion, we have exposed $30 \times 30 \times 3$ or $4 \,\mu\mathrm{m}$ deep micro-trenches in a Si sample to L-mode D discharges for a cumulative 30 s or 10 s using the DiMES facility at DIII-D. C deposition profiles on the trench floors inferred via EDS analysis were consistent with the Cion incident directions corresponding to a polar angle of $\theta \sim 60^{\circ}$ (referenced to the surface normal) and azimuthal angle of $\varphi \sim -55^{\circ}$ (referenced to the toroidal magnetic field direction) calculated by the ERO code. The thickness of deposited Clayers post-exposure was measured by AFM of the micro-trench floors and by comparing this height to the original trench surface identified by a Ga-implanted layer formed during fabrication. The C net deposition rate in an area of the microtrench floor that was shadowed from incident D ions was \sim 10 nm s⁻¹ during plasma exposure. AFM was also used to measure the Si net erosion rates, which were 3.5–5.5 nm s⁻¹ during plasma exposure. EDS was used post-exposure to measure C concentrations outside the trenches and a correlation between the C concentration and the Si erosion rate indicates erosion is suppressed by surface dilution from C impurity deposition. EDS analysis also showed that the Ga-implanted surface layers remained intact on the sloping trench wall along the toroidal direction after plasma exposure. C concentrations on this sloping wall were 40%-50% higher than concentrations on the sloping wall along the poloidal direction. Hence, C deposition may explain the significant erosion suppression on the wall along the toroidal direction. MPR calculations indicated that the C deposition rate on the wall along the toroidal direction should be higher than one along the poloidal direction by 40% for C^+ or 210% for C^{3+} incident ions due to the steeper incident angle. These results reinforce the conclusion that Cimpurity ion incident angles, which are determined by the CIADs and the PFC surface morphology, strongly affect PFC erosion rates.

Acknowledgments

The authors thank Roman Akhmechet, Zuzanna A. Lewicka, and David S. Barth for fabricating the aluminum coating, and John J. Schreiber and Guangming Cheng for their assistance with SEM/EDS/AFM analysis, in PRISM and the Imaging and Analysis Center (IAC) at Princeton University. We thank Dean Buchenauer, Josh Whaley, and Robert Kolasinski at Sandia National Laboratories for providing the Si(111) sample discs. We thank Fang Zhao and Bert G. Harrop at Princeton University for help and advice on cleaning the Si sample discs. We also thank Christopher P. Chrobak for advice on IAD predictions. This material is based upon work supported by the U.S. Department of Energy, Office of Science, Office of Fusion Energy Sciences, using the DIII-D National Fusion Facility, a DOE Office of Science user facility, under Award(s) DE-AC02-09CH11466, DE-FC02-04ER54698, DE-AC52-07NA27344, and DE-FG02-07ER54917. The authors acknowledge the use of Princeton's IAC, which is partially supported through the Princeton Center for Complex Materials (PCCM), a National Science Foundation (NSF)-MRSEC program (DMR-2011750). A.L. and J.G. acknowledge support by the U.S. Department of Energy, Office of Science, Office of Fusion Energy Sciences and Office of Advanced Scientific Computing Research through the Scientific Discovery through Advanced Computing (SciDAC) project on Plasma-Surface Interactions.

Disclaimer: This report was prepared as an account of work sponsored by an agency of the United States Government. Neither the United States Government nor any agency thereof, nor any of their employees, makes any warranty, express or implied, or assumes any legal liability or responsibility for the accuracy, completeness, or usefulness of any information, apparatus, product, or process disclosed, or represents that its use would not infringe privately owned rights. Reference herein to any specific commercial product, process, or service by trade name, trademark, manufacturer, or otherwise, does not necessarily constitute or imply its endorsement, recommendation, or favoring by the United States Government or any agency thereof. The views and opinions of authors expressed herein do not necessarily state or reflect those of the United States Government or any agency thereof.

Data availability statement

The data generated and/or analysed during the current study are not publicly available for legal/ethical reasons but are available from the corresponding author on reasonable request.

ORCID iDs

S Abe https://orcid.org/0000-0002-1477-423X J Guterl https://orcid.org/0000-0002-1049-3094 A Lasa https://orcid.org/0000-0002-6435-1884

References

- [1] Abrams T et al 2017 The inter-ELM tungsten erosion profile in DIII-D H-mode discharges and benchmarking with ERO + OEDGE modeling Nucl. Fusion 57 056034
- [2] Guterl J, Abrams T, Johnson CA, Jaervinen A, Wang HQ, McLean AG, Rudakov D, Wampler WR, Guo HY and Snyder P 2020 ERO modeling and analysis of tungsten erosion and migration from a toroidally symmetric source in the DIII-D divertor *Nucl. Fusion* 60 016018
- [3] Dux R et al ASDEX Upgrade Team 2009 Plasma-wall interaction and plasma behaviour in the non-boronised all tungsten ASDEX Upgrade J. Nucl. Mater. 390–1 858
- [4] van Rooij G J et al the ASDEX Upgrade Team, JET-EFDA Contributors 2013 Tungsten divertor erosion in all metal devices: Lessons from the ITER like wall of JET J. Nucl. Mater 438 S42
- [5] Den Harder N, Brezinsek S, Pütterich T, Fedorczak N, Matthews G F, Meigs A, Stamp M F, van de Sanden M C M, Van Rooij G J and IET Contributors 2016 ELM-resolved divertor erosion in the IET ITER-Like Wall Nucl. Fusion 56 026014
- [6] Ding R et al 2016 Simulation of gross and net erosion of high-Z materials in the DIII-D divertor Nucl. Fusion 56 016021
- [7] Xie H, Ding R, Kirschner A, Chen J L, Ding F, Mao H M, Feng W, Borodin D and Wang L 2017 ERO modelling of tungsten erosion and re-deposition in EAST L mode discharges Phys. Plasmas 24 092512
- [8] Dai SY, Yang KR, Liu DH, Shi Q, Cui B, Liu SG and Wang DZ 2021 Impacts of impurity flux on erosion and deposition of carbon/tungsten rough surfaces *Nucl. Mater. Energy* 19 100802
- [9] Guterl J, Bykov I, Sinclair G, Snyder P, Johnson C, Ennis D, Loch S, Abe S, Skinner C and Rudakov D 2021 Progress toward predictive modeling and in-situ monitoring of tungsten net erosion in tokamak divertor', Nucl. Fusion (IAEA-FEC2020), under review
- [10] Chrobak C P et al 2018 Measurement and modeling of aluminum sputtering and ionization in the DIII-D divertor including magnetic pre-sheath effects Nucl. Fusion 58 106019
- [11] Abe S et al 2021 Determination of the Characteristic Magnetic Pre-Sheath Length at Divertor Surfaces Using Micro-Engineered Targets on DiMES at DIII-D', Nucl. Fusion, under review
- [12] Mellet N, Gunn J P, Pégourié B, Marandet Y, Martin C and Roubin P 2017 Tungsten erosion by impurities and redeposition: focus on the magnetised sheath Plasma Phys. Control. Fusion 59 035006
- [13] Abe S et al 2021 Experimental Verification of Ion Impact Angle Distribution at Divertor Surfaces Using Micro-Engineered Targets on DiMES at DIII-D Nucl. Mater. Energy 27 100965
- [14] Rudakov D L et al 2009 Plasma-wall interaction and plasma behaviour in the non-boronised all tungsten ASDEX Upgrade Phys. Scr. T138 014007
- [15] Lasa A and Coburn J MPR' source code (https://github.com/ORNL-Fusion/MPR)
- [16] Lasa A et al 2016 58th Annual Meeting of the APS Division of Plasma Physics (San Jose, California, October 31–November 4 2016) (http://meetings.aps.org/link/BAPS.2016.DPP.TP10.88)
- [17] Schmid K, Mayer M, Adelhelm C, Balden M and Lindig S 2010 Impact of gyro-motion and sheath acceleration on the flux distribution on rough surfaces Nucl. Fusion 50 105004
- [18] Ziegler J F, Ziegler M D and Biersack J P 2010 SRIM—The stopping and range of ions in matter *Nucl. Instrum. Methods Phys. Res. Sect. B Beam Interact. Mater. Atoms* 268 1818–23
- [19] Ding R et al 2017 Advances in Understanding of High-Z Material Erosion and Re-deposition in Low-Z Wall Environment in DIII-D Nucl. Fusion 57 56016
- [20] Zarraoa L et al 2019 Sci. Rep. 9 16263
- [21] Coburn J et al 2019 Erosion characterization of SiC and Ti₃SiC₂ on DIII-D using focused ion beam micro-trenches Nucl. Mater. Energy 19 316–23
- [22] Behrisch R and Eckstein W 2007 Sputtering by Particle Bombardment (Berlin: Springer-Verlag GmbH)
- [23] Eckstein W Reflection (Backscattering)', IPP 17/12 August (2009)
- [24] Stangeby P C 2000 The Plasma Boundary of Magnetic Fusion Devices (Bristol: IOP Publishing)
- [25] Bykov I et al 2021 Characterization of the electric sheath by experimental measurements of ion trajectories near the tokamak divertor target', Nucl. Fusion, under review
- [26] Mutzke A, Schneider R, Eckstein W and Dohmen R 2011 SDTrimSP: Version 5.00' IPP Report
- [27] Abrams T, Bringuier S, Thomas D M, Sinclair G, Gonderman S, Holland L, Rudakov D L, Wilcox R S, Unterberg E A and Scotti F 2021 Evaluation of silicon carbide as a divertor armor material in DIII-D H-mode discharges Nucl. Fusion 61 066005
- [28] Younkin T R, Green D L, Simpson A B and Wirth B D 2021 GITR: An accelerated global scale particle tracking code for wall material erosion and redistribution in fusion relevant plasma—material interactions' Comput. Phys. Commun. 264 107885
- [29] Lasa A et al 2020 Multi-physics modeling of the long-term evolution of helium plasma exposed surfaces Phys. Scr. 2020 014041